BACHELOR THESIS

Addressing hyperfine structure in BaF towards laser cooling

Author:
Izabella Thompson

First examiner:
Prof. dr. Steven HOEKSTRA

Second examiner:
dr. Kristof de BRUYN

A thesis submitted in fulfillment of the requirements
for the degree of Bachelor of Science

in the

Van Swinderen Institute for Particle Physics and Gravity

July 9, 2022

UNIVERSITY OF GRONINGEN

Abstract

Addressing hyperfine structure in BaF towards laser cooling

by Izabella Thompson

The NL-eEDM experiment aims to use a slow and intense molecular beam of barium fluoride (BaF) to enable a competitive measurement of the electron electric dipole moment (eEDM). A molecular beam of BaF is generated in a cryogenic buffer gas source and decelerated by a Stark decelerator. The beam that exits the decelerator spreads out with a transverse velocity of $\pm$ 5m/s. However, the divergence of the molecular beam should be sufficiently counteracted such that the beam can fit the constraints of the remaining part of the experimental setup. A number of lasers will be used to exert a force on the molecular beam in the transverse direction, in a technique called Doppler cooling or optical molasses.

However, a large number of photons need to be scattered in order to achieve an effective force, for which the $A^2\Pi_{1/2}(v = 0, N = 0, J = 1/2)$ to $X^2\Sigma^+(v = 0, N = 1)$ transition will be used. The molecules in the excited state can decay to any one of the four hyperfine levels of the ground state. The current laser induced fluorescence detection setup addresses only one of these four hyperfine levels. Therefore, the remaining three hyperfine levels are considered dark, which makes them a leak in the cooling cycle. The work presented in this thesis targets the second hyperfine level of the ground state such that the loss of molecules to unaddressed levels is reduced. This presents a step towards the laser cooling of BaF, with the remaining two ground hyperfine levels left to be coupled to the $A^2\Pi_{1/2}$ excited state. The vibrational $v = 1$ and $v = 2$ levels can then be addressed with repump lasers to ensure a vibrationally closed cycle.

Contents

Chapter 1

Introduction

The Standard Model of Particle Physics (SM) is the theory which describes the weak, electromagnetic and strong force [1]. These interactions, along with gravity, are currently used to interpret the universe and the physics which governs it. Furthermore, the SM provides all of the known elementary particles and is able to classify them. By the 1970s, the SM was considered complete and has been verified by many experiments, including the discovery of the top quark, which had been predicted by the model [2]. The model is able to describe how particles are composed of quarks and as such can be either baryons or leptons. These particles are under the influence of forces which are carried by particles known as gauge bosons [3]. The weak force is mediated by the $\mathcal{Z}$ and $\mathcal{W}$ bosons, the electromagnetic force by the photon and the strong interaction by the gluon. Gravity however, is nowhere to be found in the SM [4].

As gravity is a force which is so fundamental in physics, it is surprising that the SM cannot adequately describe it. This follows from gravity being interpreted in the classical framework and as such any quantum description has yet to be experimentally verified [5]. However, it is not just gravity for which the SM falls short, the model cannot describe phenomena such as there being more matter than antimatter in the universe or the inclusion of dark matter [6].

The SM must obey $\mathcal{CPT}$ symmetry. $\mathcal{CPT}$ stands for charge conjugation, parity and time reversal [7]. These are transformations, which when all three are applied, leaves the model invariant. Therefore, a violation in time reversal symmetry means that there is a violation in $\mathcal{CP}$ symmetry [8]. The SM does allow for $\mathcal{CP}$ violation with some arising from the complex phase of the CKM matrix [9]. Therefore, if the magnitude of such a $\mathcal{CP}$ violating system is larger than that which is predicted by the SM, this would point towards extensions of the model which can explain this difference [10]. The predicted EDM of the electron by the SM is extremely small with order 10^{-38} $e \cdot$ cm [11]. Measuring this experimentally requires precision, however in some of the extensions of the SM, the predicted eEDM value can be orders of magnitude larger. Some of these values are within experimental reach given the current measurement techniques and so finding such a value would indicate new physics.

Chapter 2

Theory

2.1 Electric dipole moment of the electron

Classically, an electric dipole is the separation, $\vec{r}$ between two opposite point charges, $-q$ and $+q$ such that the electric dipole moment (EDM) is given by $q\vec{r}$. The search for a permanent EDM in fundamental particles such as the neutron and electron forms a prominent part of the research in precision physics [10]. Under the parity transformation $\mathcal{P}$, the EDM flips sign with its spin left unchanged as shown in Figure 2.1. The EDM can be considered as the distribution of charge and so a time reversal transformation $\mathcal{T}$, will leave this unchanged and instead reverse the spin of the particle. A violation $\mathcal{T}$ symmetry, means that by $\mathcal{CPT}$ conservation $\mathcal{CP}$ is also violated.
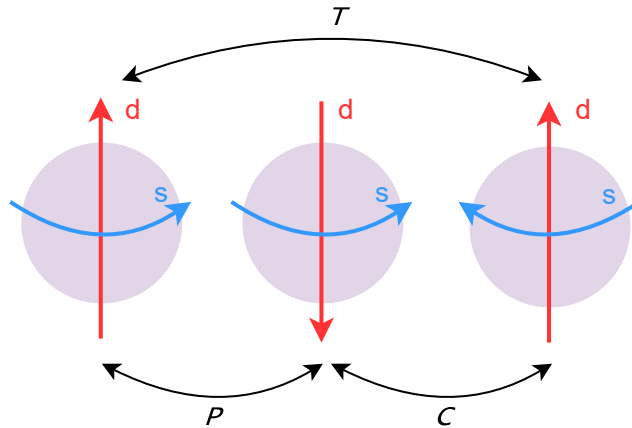

FIGURE 2.1: Transformations of $\mathcal{C}$, $\mathcal{P}$ and $\mathcal{T}$ on a fundamental particle with spin, s and electric dipole moment d.

Experimental observation of an EDM which is greater than that which predicted by the SM, would point to certain extensions of the SM which are able to account for this value. Figure 2.2 shows extensions of the SM as well as the proposed limit obtained from measuring the electric dipole moment of the electron for this experiment. Fundamental particles such as the electron can be used as a probe for symmetry violation in the search for new physics.

To experimentally determine the EDM of the electron, the electron is subject to an electric field which is aligned either parallel or antiparallel to an applied magnetic field [13]. The energy shift that occurs due to the change in orientation of the electric field is what is measured. Details of how the EDM measurement is extracted can be found in [14]. However due to its charge, subjecting a bare electron to an electric field results in the Lorentz force acceleration of the particle, which complicates taking a measurement. Therefore in eEDM measurements, a molecule with an single unpaired electron in its outer shell is used to overcome this problem of acceleration.
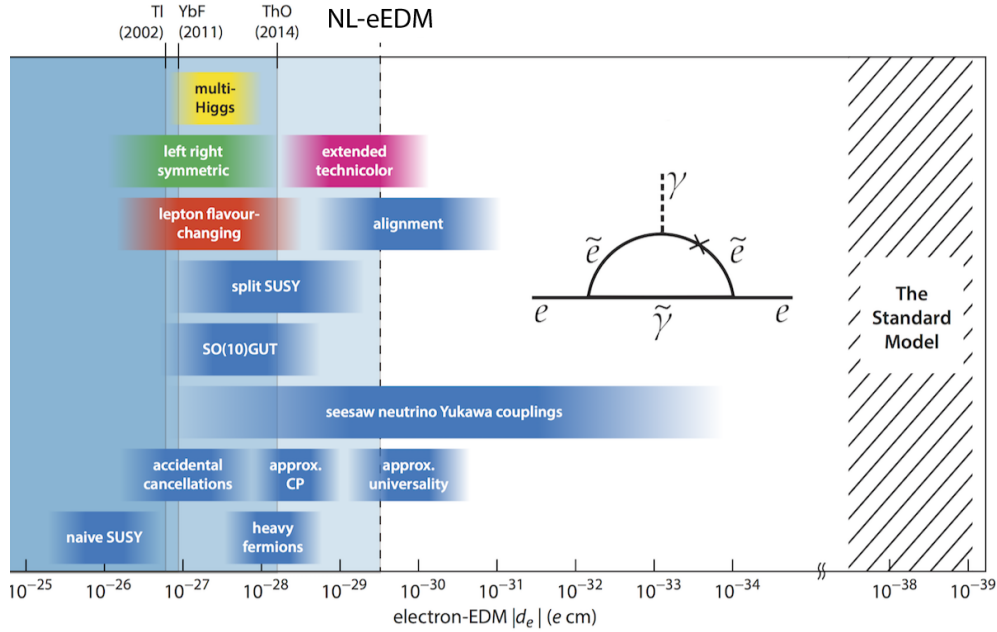
FIGURE 2.2: Extensions of the SM along with limits on the eEDM from other experiments are indicated at the top of the Figure. The limit proposed with this experiment is indicated with a dashed line. Figure from [12].

2.2 The NL-eEDM experiment

Several molecules have been used to obtain an experimental limit on the eEDM, including YbF and ThO[15][16]. The choice of molecule depends on which source of a $\mathcal{CP}$ violating process is being studied. A molecule which is polar, paramagnetic and contains a heavy atom results in an enhancement factor of the eEDM [17][18]. The enhanced sensitivity of such a molecule to the eEDM is given by a parameter called the effective electric field E_{eff}. This enhancement factor is due to the electron passing by the strong internal electric field of the nucleus [12]. As the E_{eff} scales with atomic number Z^3 heavy atoms are preferred [19].

The NL-eEDM experiment uses the molecule barium fluoride (BaF) as a probe for measuring the electric dipole moment of the electron. The choice of molecule varies between different EDM experiments depending on which properties are optimum for each experimental setup. The statistical uncertainty on an eEDM measurement is given by equation 2.1

$$\sigma_{\mathrm{d}} = \frac{\hbar}{e} \frac{1}{2|P|E_{eff}\tau\sqrt{\dot{N}T}} \tag{2.1}$$

Where $|P|$ is the polarisation factor, $\dot{N}$ the counting rate, T the measurement time and τ the coherent interaction time of the molecules with the electric field. To lower the uncertainty, τ can be increased. Although BaF has a smaller enhancement factor than both YbF and ThO, the NL-eEDM experiment uses Stark deceleration to increase the time spent in the electric field given by τ. The BaF molecular beam is produced by a cryogenic buffer gas source shown in Figure 2.3 and is focused into the decelerator by an electrostatic hexapole. When the molecules enter the travelling wave Stark decelerator, they have a longitudinal velocity of approximately 180 m/s. The longitudinal velocity of the beam is decelerated to 30 m/s by the 4.5 m decelerator. Upon leaving the decelerator, the beam spreads out with a transverse velocity of approximately ±5 m/s. A cold, parallel beam of molecules is required for the second half of the experiment which takes the measurement of the eEDM itself. Therefore, the transverse velocity spread of the beam needs to be reduced such that the beam can fits the constraints of the second half of the experiment.
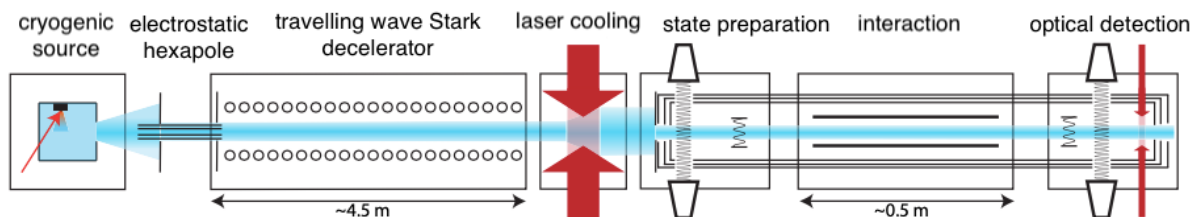
FIGURE 2.3: The proposed experimental setup for the NL-eEDM experiment. BaF molecules are produced in the cryogenic source and focused into the travelling wave Stark decelerator by an electrostatic hexapole. For the molecular beam to be used in remaining half of the experiment, the transverse velocity of the beam is reduced by laser cooling. Figure from [12].

2.2.1 BaF source and travelling wave Stark decelerator

Molecules of barium fluoride are generated within a copper cell containing a rotating cylindrical target of barium. This cryogenic cell can be seen in Figure 2.4. The target of barium is ablated using a pulsed laser of wavelength 532 nm. The gases sulfur hexafluoride (SF6) and neon (Ne) are injected into the cell such that barium reacts with the SF6 resulting in new products including BaF. Keeping the cell at a temperature of 17 K and optimising the flow of the two gases into the cell, ensures a beam of BaF is carried out of the cell by the Ne buffer gas. Molecules are detected upon exit of the cell by absorption on the strong transition seen in Figure 2.7.
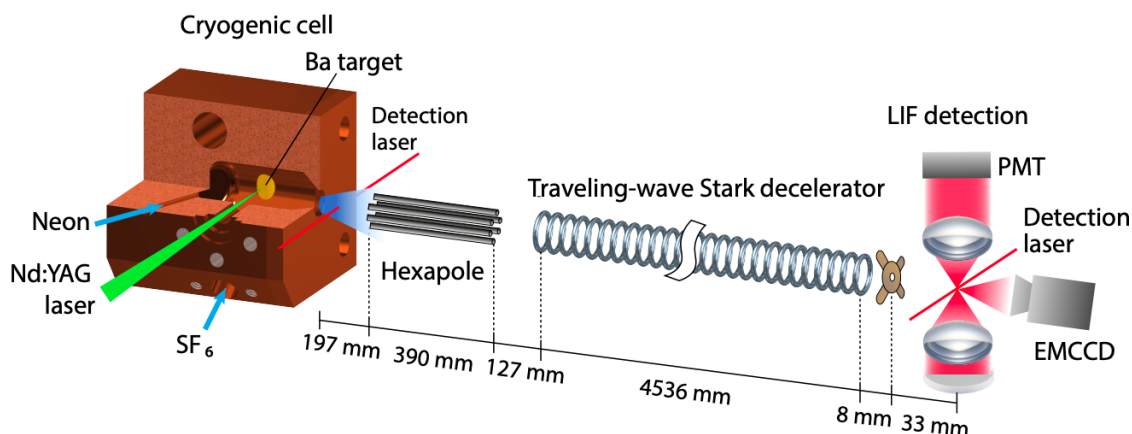

FIGURE 2.4: The setup used to provide a slow and intense beam of BaF molecules. BaF molecules are produced in the cryogenic cell and focused into the decelerator by an electrostatic hexapole. The molecules are decelerated and subsequently detected by laser induced fluorescence. A lens system focuses light onto a PMT with an EMCCD camera used to image the beam. Figure made by Joost W. F. van Hofslot.

The molecular beam is guided into the decelerator using an electrostatic hexapole. This works as a focusing lens, directing molecules with large transverse velocities into the phase space of the Stark decelerator. A time-varying high voltage electric field is applied to the electrodes within the decelerator [20]. This produces a three dimensional trapping potential which can move and therefore be used to trap and decelerate molecules in low field seeking states. Figure 2.5 shows the electric field strength with position in the decelerator. The black circles represent the electrodes with a traps given by the areas of low field strength (blue).

The number of molecules which leave the decelerator can be determined by a second detector laser. The frequency of the detection laser is such that the molecules of BaF are excited and subsequently decay, emitting a photon. The light from this laser induced fluorescence (LIF) is focused onto a PMT by a lens system as seen in Figure 2.4. A EMCCD camera is used to image the beam at the end of the decelerator.
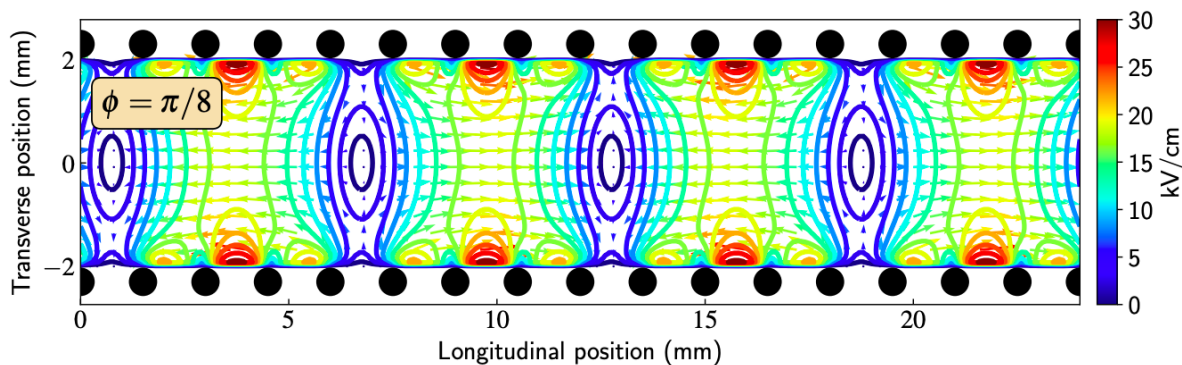
FIGURE 2.5: The electric field strength inside of the decelerator with regions of high and low field used to trap molecules in low field seeking states. The black dots represent the electrodes where a time-varying high voltage is applied. Figure from [21].
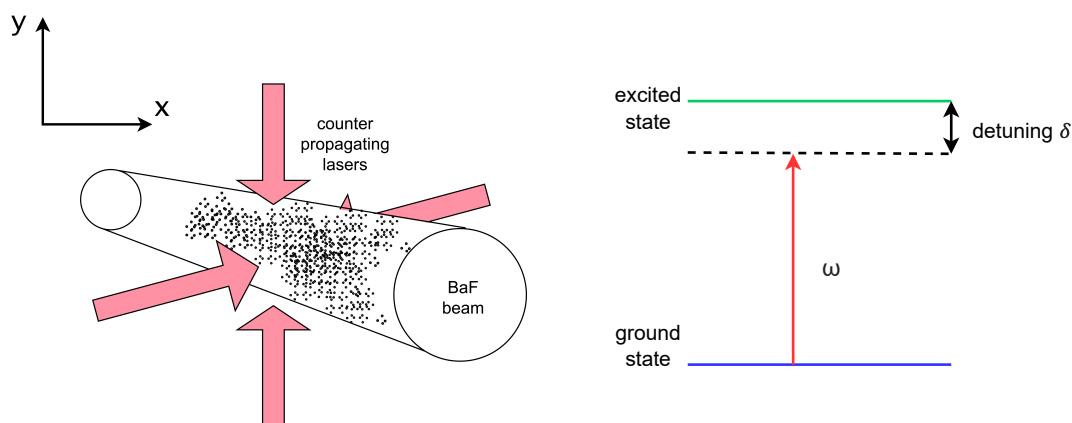
2.3 Laser cooling

FIGURE 2.6: **a)** The 2D optical molasses implemented for the laser cooling of a molecular beam of BaF. **b)** A red-detuned laser of frequency ω is chosen such that molecules approaching the laser are on resonance. The detuning is given by δ. Figure adapted from [22].

The transverse velocity spread of the molecular beam of BaF needs to be reduced to provide a parallel beam to the second half of the experiment. In order to stop this spread a force is applied. This can be done with lasers in a process known as Doppler cooling. Two pairs of identical counter propagating lasers are used to cool in both x directions and y directions as shown in Figure 2.6a and is known as a 2D optical molasses [23]. Each laser is tuned at the same frequency which corresponds to a transition in the molecule. However, this frequency is lowered to a value of ω which is just below the resonant frequency of the transition. This light is then said to be red-detuned by an amount δ as shown in Figure 2.6b. The transfer of momentum between the molecule and a photon of the laser is the principle behind laser cooling. When a molecule absorbs a photon from the laser and excites, it subsequently decays emitting a photon in a random direction and recoiling [24]. The red-detuning of the laser means that molecules are more likely to absorb photons from a beam which is moving in the opposite direction to the molecule itself. Therefore, over many of these events called scatterings, the beam loses energy in the transverse direction.

The molecular beam of BaF leaves the decelerator with a transverse velocity of ± 5 m/s. For the transition of $A^2\Pi_{1/2} \leftarrow X^2\Sigma^+$, the recoil of one photon is approximately 3 mm/s [23]. Therefore, nearly 2000

photon scatterings per molecule are needed to completely dissipate this transverse velocity. A high scattering rate is required to cool the beam effectively in the relatively short distance of the cooling chamber. Given that the lifetime τ of the $A^2\Pi_{1/2}$ excited state is $\sim$ 57 ns, then the natural line width Γ of the transition is $1/2\pi\tau$ = 2.8 MHz [25]. In the ideal case, the scattering rate is perfect such that the total scattering time is $\sim$ 700 μs. With the longitudinal velocity of the beam decelerated to 30 m/s, the required length of the light field needed to cool the beam is $\sim$ 20 mm. Work done by J. Almond suggests that the scattering rate R_γ due to imperfect scattering that we can apply to our transition is $2\Gamma/5$ [26]. From this, the length of the light field required is $\sim$ 6 cm. To improve the scattering rate of photons per molecule, decays to other vibrational levels should be considered as well as any hyperfine structure.

2.3.1 Molecular structure of BaF

A molecule selected for laser cooling has several important attributes including a short lifetime of the excited state such that a high spontaneous emission rate results in a large number of scattered photons. The decay of a molecule to a different vibrational level of the ground state with respect to the vibrational level of the excited state, can be described by its Franck-Condon factors. Branching to other vibrational levels is unlikely if a molecule has highly diagonal Franck-Condon factors. This results in a closed vibrational cycle as molecules are not lost to these dark vibrational states.

For the laser cooling of BaF, the transition from the $N = 1$ rotational and $v = 0$ vibrational level in the electronic ground state ($X^2\Sigma^+$) to the $N = 0$, $v = 0$ electronic excited state ($A^2\Pi_{1/2}$) has been selected [27]. This transition is shown in Figure 2.7a. The wavelength of light required to excite the molecule
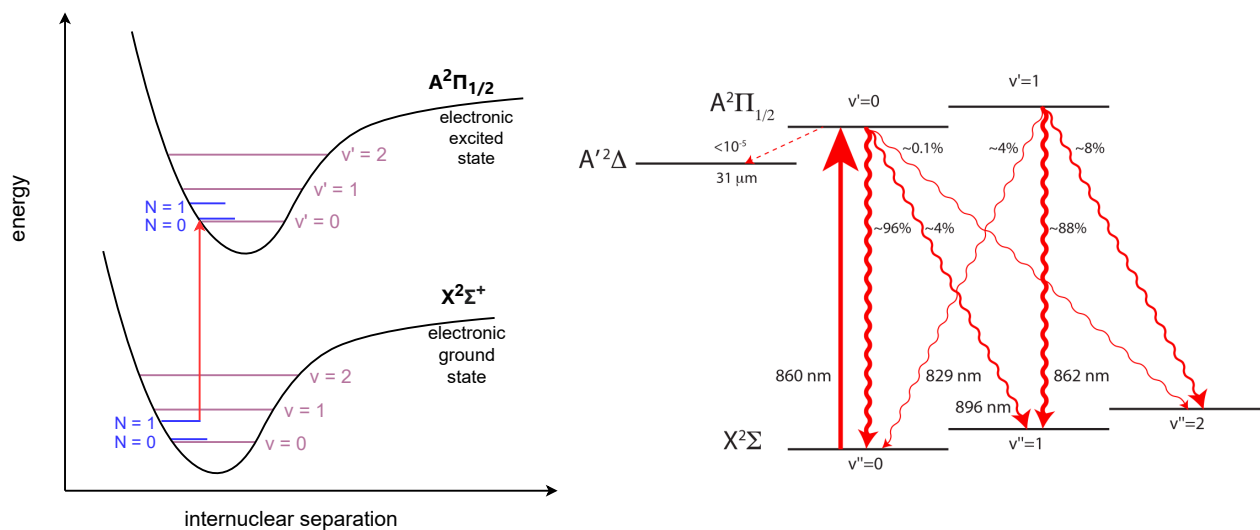

FIGURE 2.7: **a)** The transition from the $X^2\Sigma^+$ electronic ground state ($N = 1$, $v = 0$) to the $A^2\Pi_{1/2}$ ($N = 0$, $v = 0$) excited state identified for the laser cooling of BaF. **b)** A cycling scheme for the laser cooling of BaF. A laser of wavelength 860 nm drives the transition of $A^2\Pi_{1/2} \leftarrow X^2\Sigma^+$, with branching ratios to other vibrational ground states indicated by percentages. Figure from [12].

from the $A^2\Pi_{1/2} \leftarrow X^2\Sigma^+$ transition is 860 nm, as shown in Figure 2.7b. The Franck-Condon factors of this transition are highly diagonal, ensuring that there are few leaks of molecules to other vibrational states. For BaF, the probability for a molecule in the $A^2\Pi_{1/2}$ excited state to decay to the $v = 0$ vibrational state is 96% given by the Franck-Condon factor of f_{00}= 0.96 [28] as seen in Figure 2.7b. Although only a small percentage of molecules in the excited state will decay to the $v = 1$ and $v = 2$ states, due to the high number of scatterings required for cooling, lasers are needed to re pump molecules back to the excited $A^2\Pi_{1/2}$ ($N = 0$, $v = 0$) state. Therefore, potential leaks of excited molecules decaying to dark, vibrational levels of the electronic ground state can be addressed.

Another consideration for optical cycling is the structure and substructure of the hyperfine levels involved in the transition, these are shown in Figure 2.9. In the ground state of BaF there are four hyperfine levels in total from the $J = 3/2$ and $J = 1/2$ levels of the fine structure splitting, these are $F = 2, 1, 0, 1$. Each of these hyperfine levels is split into m_F states which range from F to $-F$ in integer steps. The behaviour of the m_F states is particularly important in the travelling wave Stark decelerator. The high voltage applied to the electrodes of the Stark decelerator varies with time such that a three dimensional potential can trap and then slow the molecules. Each of the m_F levels is Stark shifted in the decelerator such that a negative Stark shift corresponds to a decrease in energy for increasing electric field. Therefore molecules in these states are attracted to the high voltage electrodes and are known as high field seeking states (HFS). For positively Stark shifted m_F states, an increase in electric field strength results in an increase in energy such that the molecules in this state are attracted to the electric field minima i.e the low field seeking states (LFS) [20]. The Stark shift of each ground state m_F level is shown in Figure 2.8.

Therefore, only molecules in LFS states are attracted to the minima of the three dimensional potential in the decelerator. The hyperfine level $F = 2$ contains three LFS states, $|m_F| = 1$ and $m_F = 0$ and the $F = 1$ hyperfine level of $J = 3/2$ has just one LFS state of $m_F = 0$. As BaF molecules which exit the decelerator will be in one of these four m_F states, to see an initial increase in the detection signal from LIF, the states of $F = 2$ and $F = 1$ of $J = 3/2$ can be targeted.
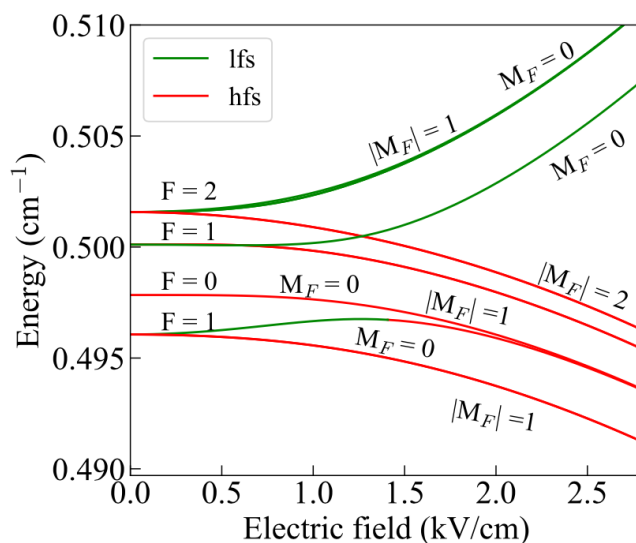

FIGURE 2.8: The Stark shift of m_F states in the hyperfine levels of the electronic ground, $N = 1$ rotational and $v = 0$ vibrational level of BaF. Molecules that enter the decelerator are energy shifted such that only low field (LFS) components (green) are trapped by the decelerator. High field seeking (HFS) m_F states (red) are attracted to the electrodes in the decelerator. Figure from [29].

A BaF molecule in the excited state of $A^2\Pi_{1/2}$ has the probability to decay to any of the four hyperfine levels of the ground state and so all four of these levels should be addressed. Molecules must be excited from each of these hyperfine levels in order to prevent dark states from occurring. To target the hyperfine structure of BaF, four lasers of differing frequency are used to excite molecules to the excited state. Figure 2.9 shows the molecular structure of BaF relevant for the chosen cooling transition. The fine structure splitting of the ground ($N = 1$, $v = 0$) state results in two total angular momentum J levels, $J = 1/2$ and $J = 3/2$. The interaction between the nuclear spin I and each total angular momentum value of J is given by $F = I + J$, where F is the hyperfine splitting. Resulting in the formation of four substates of the ground state.
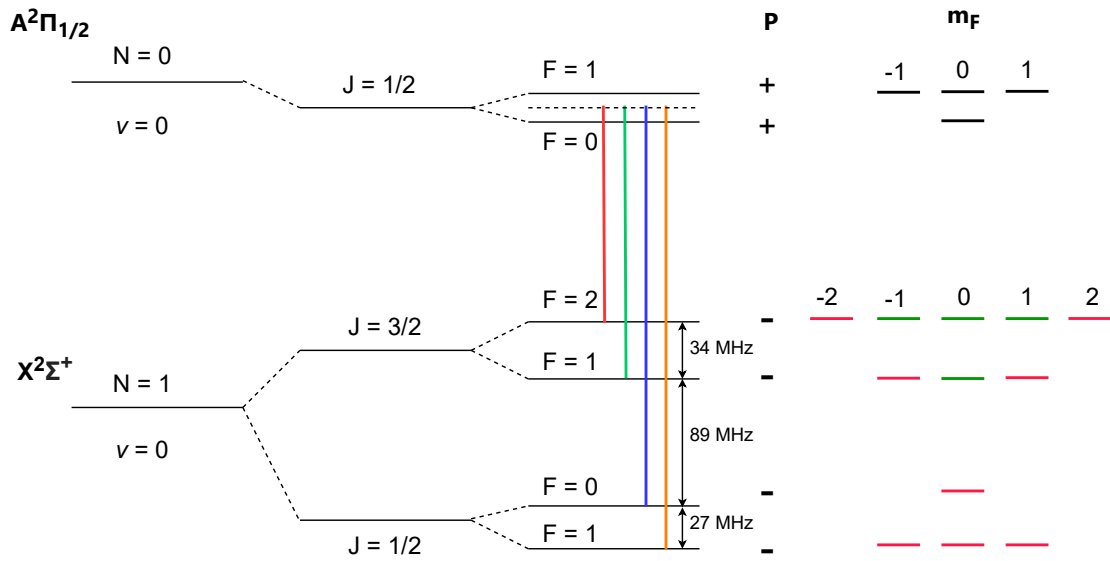
FIGURE 2.9: The transition $A^2\Pi_{1/2} \leftarrow X^2\Sigma^+$ chosen in BaF for optical cycling. The $v = 0$, $N = 1$ rotational level of the electronic ground state ($X^2\Sigma^+$) is excited to the $v = 0$, $N = 0$ rotational level of the electronic excited state ($A^2\Pi_{1/2}$). At the end of the decelerator molecules are only in a low field seeking (LFS) m_F states (green). There are no molecules in a high field seeking (HFS) m_F states as these are attracted to the electrodes in the decelerator. The parity P of each hyperfine level is indicted by (+/-). Four different laser frequencies (red, green, blue, orange) are needed to excite molecules back to the excited state.

Similarly, the $A^2\Pi_{1/2}$ excited state has a $J = 1/2$ level which then forms two hyperfine levels of $F = 1$ and $F = 0$. The splitting between these two states is assumed to be covered by the power broadening of the laser such that molecules can excite to either one of these levels.

Due to the travelling wave Stark decelerator, BaF molecules are only in the LFS m_F states indicated in green as in Figure 2.9. It is therefore ideal to target this state first, as a greater change in the fluorescence detection should be seen. However, transitions between m_F levels are governed by the selection rules $\Delta m_F = 0, \pm 1$. Linearly polarised light is used as more m_F states are addressed, however molecules in the $m_F = 2$ and $m_F = -2$ states cannot be excited due to these selection rules and therefore become dark states. Over repeated scatterings this becomes a prominent leak in the optical cycle. Addressing these dark states can be done by switching between linearly and circularly polarised light or by applying a small magnetic field to destabilise the dark states.

Chapter 3

Addressing hyperfine levels

3.1 Motivation and objective

Addressing the hyperfine levels in the ground state of BaF allows for more efficient fluorescence detection as well as a move towards repeated optical cycling. The laser cooling of BaF would mean that the transverse velocity of the beam which leaves the decelerator could be reduced. The molecular beam is therefore able to fit the constraints of the remaining part of the experimental setup.

Previously, the molecule strontium fluoride (SrF) was used in the NL-eEDM experiment as the molecule has been well studied with respect to deceleration and laser cooling. Although both BaF and SrF are similar in their molecular structure, the number of fluorescence counts by LIF at the end of the decelerator is much lower for BaF than for SrF. An improvement in fluorescence signal would mean that the effect of changing various parameters to improve the number of molecules could be better understood. Four different frequencies to target the four ground hyperfine levels are required. For SrF an EOM was used to target the hyperfine levels as the hyperfine structure was symmetric. However, the asymmetry in the splitting of the ground hyperfine levels of BaF as seen in Figure 2.9, requires the use of an acoustic optic modulator (AOM) for each hyperfine level instead.
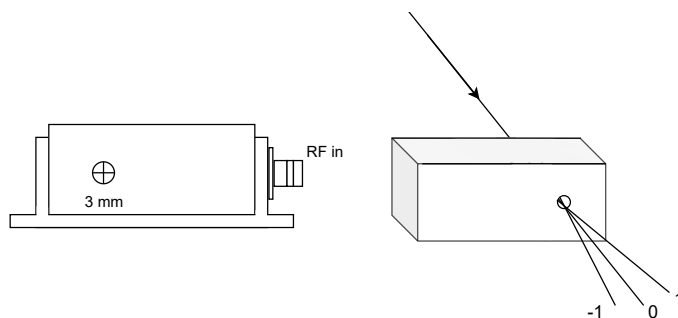
3.2 AOM: acoustic optic modulator

FIGURE 3.1: **a)** A sketch of the AOM (AOMO 3080-122) used for the setup. An oscillating radio frequency (RF) is used to drive a piezoelectric transducer which is in contact with a tellurium dioxide crystal (TeO2). Acoustic waves are produced inside the crystal and a laser is focused through a 3 mm hole into the AOM. **b)** The laser diffracts off this acoustic wave into different order beams, only zero and first order beams are indicated.

An AOM is able to shift the frequency of light by diffraction off an acoustic wave [30]. A sketch is given in Figure 3.1a where an oscillating radio frequency (RF) is applied to a piezoelectric transducer. The piezoelectric transducer is in contact with a material, in this case a tellurium dioxide crystal such that an acoustic wave propagates through the crystal. The acoustic wave changes the refractive index of the crystal in different regions periodically through the compression and rarefaction of the material [31]. A laser enters the AOM perpendicular to the acoustic wave propagation and diffracts off these regions of

different refractive index. The light therefore splits into orders of diffraction as seen in Figure 3.1b. The first order beams +1 and -1 are shifted by plus and minus the input frequency respectively. Second order beams are shifted by twice this frequency with higher orders following the same pattern.
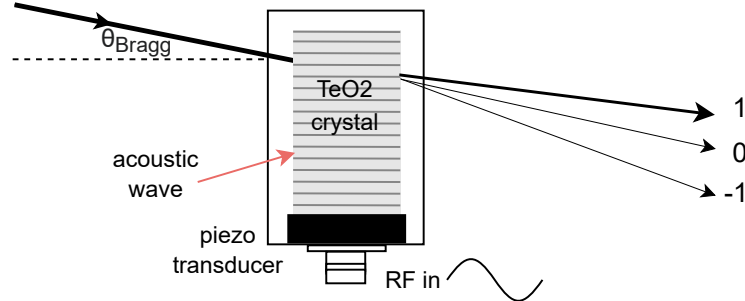

FIGURE 3.2: The angle between the incident laser beam and the normal of the AOM surface forms the Bragg angle. The zeroth order beam has the same frequency as the incoming laser with the first order beams shifted by either plus or minus the frequency applied at the RF input.

In order for diffraction to occur, light enters the AOM at the Bragg angle shown in Figure 3.2. This is the angle between the normal of the surface of the AOM and the incident beam and is given by:

$$\theta_{\text{Bragg}} = \frac{\lambda f}{2v} \tag{3.1}$$

Where λ is the wavelength of light entering the crystal, f the frequency of the RF signal and v the velocity of the acoustic wave through the crystal. For this work, a shift in frequency of +89 MHz to a laser of wavelength 860 nm was required to target the $F = 0$ hyperfine level of the ground state as seen in Figure 2.9. For a TeO2 crystal, the velocity of an acoustic wave v is 4.2 mm/µs [32]. Imputing these values into the equation for order separation gives:

$$\theta_{\text{sep}} = \frac{\lambda f}{v} \sim 0.9° \tag{3.2}$$

To obtain the positive frequency shifted part of the beam, the first order (+1) should be picked off from the zeroth order. With a small angle of separation between orders, both alignment and the splitting off of the beams is difficult due to the high sensitivity of the AOM to changes in angle. Therefore, the beam which leaves the AOM can be made to propagate over a relatively large distance such that the orders diverge. To minimise the loss of power due to the laser propagating through the AOM, the diffraction efficiency should be optimised. The diffraction efficiency is the ratio between the power incident on the AOM P_0 and the power in a specific diffracted order m:

$$DE = \frac{P_m}{P_0} \tag{3.3}$$

Ideally, all of the incident power is directed to the first order as this is the order with the required frequency. However, typically only 50% of the optical power can be diffracted for a sufficiently high power applied to the AOM [30]. Efficiency is improved by increasing the period between the regions of compression and rarefaction in the crystal. In this way, higher order solutions of the grating equation are removed. For a relatively small surface area where the beam can enter the AOM, it is important that the beam is focused into the crystal. This can be done using a pair of lenses either side of the AOM to focus the light and then to ensure the beam is made parallel again.

3.3 Configuration of optics

An optical setup which targets both the $F = 0$ and $F = 1$ hyperfine levels of the ground state in BaF is shown in Figure 3.3. A titanium-sapphire laser (Ti:Sa) is set at a frequency which targets the $F = 1$ level shown in Figure 2.9. A polarising beam splitting cube (PBSC) splits off vertically polarised light and allows horizontally polarised light to pass through. The half-wave plate before PBSC1 is able to split the vertically polarised light from the laser into vertical and horizontal components. The vertically polarised light is sent to the $F = 1$ path and horizontal to the $F = 0$ path. The combination of half-wave plate and PBSC allows for control over the power sent to each path.

A lens before and after the AOM indicated by +89 MHz allows for focusing into the AOM and then making the beam parallel once more. The first (+1) order is reflected by a D-shaped mirror (indicated with *) such that the zeroth order path can pass by the mirror and be dumped. The paths of $F = 0$ and $F = 1$ are recombined by PBSC3 and the light is eventually sent to both absorption (ABS) and laser induced fluorescence (LIF) detection by coupling into two fibre ports. A monitoring cavity is used to check if the combined beam contains both modulated (+89 MHz) and unmodulated (+0 MHz) frequencies.
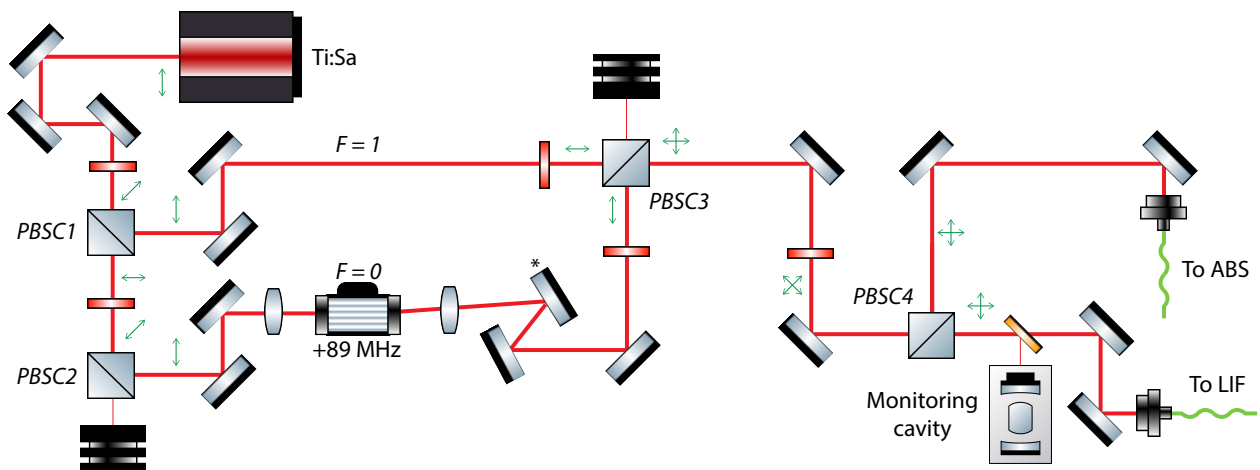

FIGURE 3.3: Optical setup used for targeting the $F = 0$ and $F = 1$ hyperfine levels of the ground state in BaF. The frequency of the Ti:Sa laser addresses the $F = 1$ level. A polarising beam splitting cube (PBSC) is used to split some of the beam to the AOM indicated with +89 MHz. This is the frequency shift required to target the $F = 0$ hyperfine level. A D-shaped mirror (indicated with *) results in the zeroth order being dumped and the first order (+1) reflected and combined with the beam from $F = 1$ by a PBSC. Light is sent to the absorption (ABS) and laser induced fluorescence (LIF) detection. Figure made by Joost W. F. van Hofslot.

3.4 Confocal optical cavity

To check if the frequencies that we expect are in the final beam, a confocal optical cavity can be used. The cavity consists of two parallel mirrors between which light undergoes multiple reflections. One of the mirrors is attached to a piezo such that different frequencies are resonant in the cavity at specific distances. The path of such a light ray is shown in Figure 3.4, where the incoming beam is reflected three times, with some transmission at the second mirror before returning to the initial position on the first mirror. The arrangement of mirrors in Figure 3.4 is confocal meaning that the radius of curvature of both mirrors is equal to the length of the cylindrical cavity L. Such a configuration results in low sensitivity to misalignment into the cavity as the centre of the radius of curvature continues to lie along the surface of each mirror even with changes in the angle of the mirrors [33].
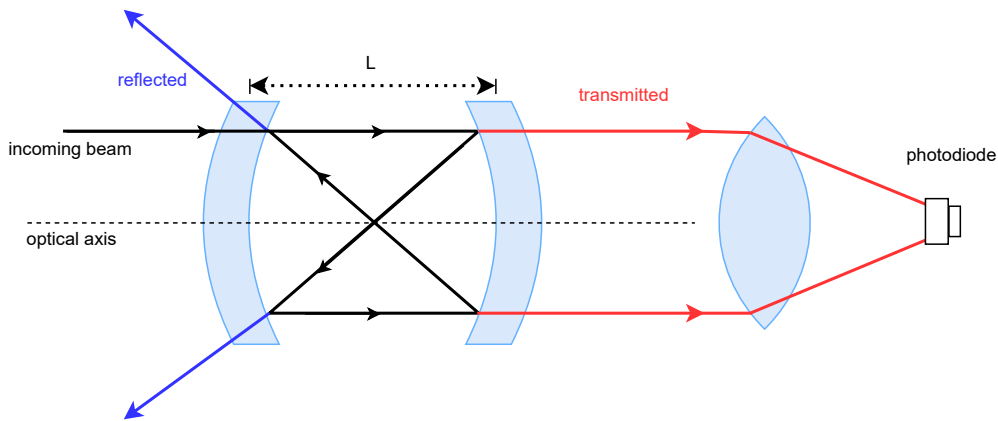
FIGURE 3.4: Inside a confocal optical cavity both mirrors have the same radius of curvature which is equal to the length L of the cavity. Transmitted light is an integer multiple of 2π and is focused by a lens onto a photo diode at the end of the cavity.

Once returning to the same position where the beam entered the cavity, the reflected light can interfere constructively or destructively with the incoming beam. For optical resonance to occur within the cavity, the light interferes constructively such that the optical phase change is an integer multiple of 2π [34]. Multiple wavelengths which satisfy this condition are the eigenmodes, or modes of the cavity [35]. The transverse electromagnetic mode numbers are given by n and m which lie in two perpendicular directions in the plane orthogonal to the optical axis [36]. Light which enters along the optical axis and interferes constructively produces longitudinal modes with mode order q. The mode structure within the cavity is given by the resonant optical frequencies [37]:

$$\nu_{nmq} = q\Delta\nu_{FSR} + (n+m)\delta\nu \tag{3.4}$$

The first term corresponds to longitudinal frequencies, where $\Delta\nu_{FSR}$ is the frequency difference between consecutive longitudinal resonances known as the free spectral range (FSR) [38] and can be expressed in the following way:

$$FSR = \frac{c}{2L} \tag{3.5}$$

Where $\lambda = 2L/n$ and n is the density of the medium in the cavity which in this case is air with c being the speed of light. The factor of 2 comes from the light traversing a distance of $2L$ before constructively interfering. Transverse modes travel double this distance.
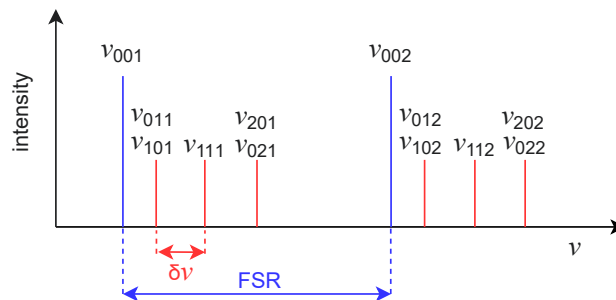

FIGURE 3.5: The modal frequencies produced in an optical cavity with longitudinal q and transverse modes n and m indicated in blue and red respectively. Each frequency is denoted with ν_{nmq}. The separation of longitudinal modes q and $q+1$ is given by $\Delta\nu_{FSR}$, the free spectral range. The spacing between transverse modes is $\delta\nu$. Figure adapted from [39]

The spacing between transverse modes is given by $\delta \nu$. Figure 3.5 shows the FSR between two consecutive longitudinal modes, $q = 1$ and $q = 2$ (blue). The first transverse mode (red) following a longitudinal mode has n and m equal to either 1 or 0 as seen in Figure 3.5. The amplitude of the standing wave pattern developed within a cylindrical cavity is described by the Laguere–Gaussian polynomial and represents the higher order transverse modes [36]. From both experimental and theoretical work, it has been found that even small deviations in the cylindrical symmetry of the system breaks the degeneracy of the Laguere–Gaussian polynomials, resulting in the non-degenerate Hermite-Gaussian polynomials which describe a rectangularly symmetric system [40]. Deviations can occur from factors such as an asymmetry in mirror coating or alignment into the cavity. Implementing an aperture at the entrance of the cavity reduces the development of transverse modes.

Chapter 4

Results

4.1 Diffraction efficiency

The AOM[1] used in this work was specified as having a diffraction efficiency of up to 80% [32]. Therefore, the power incident on the AOM as well as the power directed to the first order was measured for increasing RF power applied to the AOM. Figure 4.1 shows that when RF power is increased, the diffraction efficiency increases to 45% until the curve begins to saturate at approximately 30 dBm. As a maximum efficiency is obtained when the RF power is equal to this saturation value [41], the AOM was powered at 30 dBm for the remaining measurements. The diffraction efficiency can be improved further by optimising the size of the beam waist at the centre of the crystal or the angle at which the beam enters the AOM.
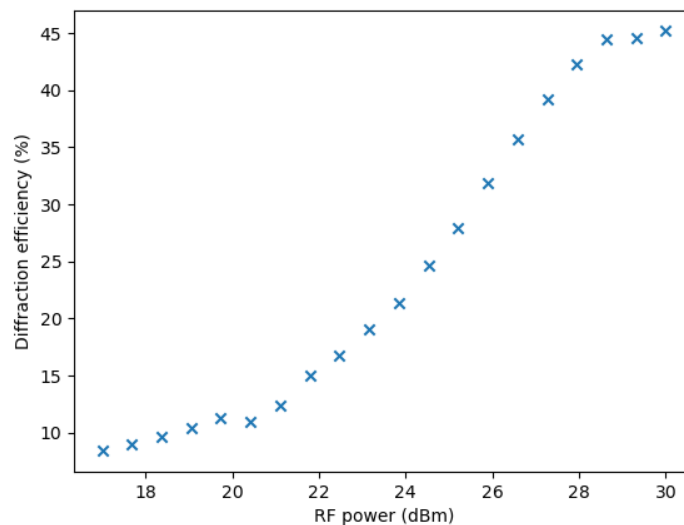

FIGURE 4.1: Diffraction efficiency of the AOM (AOMO 3080-122) as a function of RF power applied to the crystal. The alignment of the beam into the AOM gave a maximum efficiency of 45% with power saturation occurring at ~ 30 dBm.

4.2 Optical cavity

The modulated (+ 89 MHz) and unmodulated (+ 0 MHz) beams were coupled into a confocal optical cavity[2]. The cavity was scanned with a sawtooth signal and the transmitted light detected by a photodiode at the end of the cavity. The results are shown in Figure 4.2. The output signal of the photodiode shows

---

[1] AOMO 3080-122
[2] Thorlabs SA200-6A

two longitudinal modes and approximately five transverse modes in one scan range. The dip seen at $\sim$ 4.8 GHz indicates the end of the scan range of the piezo. The modes corresponding to the modulated and unmodulated beams were identified by blocking the respective beams on the laser table and observing the change in number of modes seen on an oscilloscope which was connected to the cavity. To ensure that two longitudinal modes were correctly observed per scan, the cavity was scanned using a triangular wavefunction with the spectrum shown in Figure 4.3.
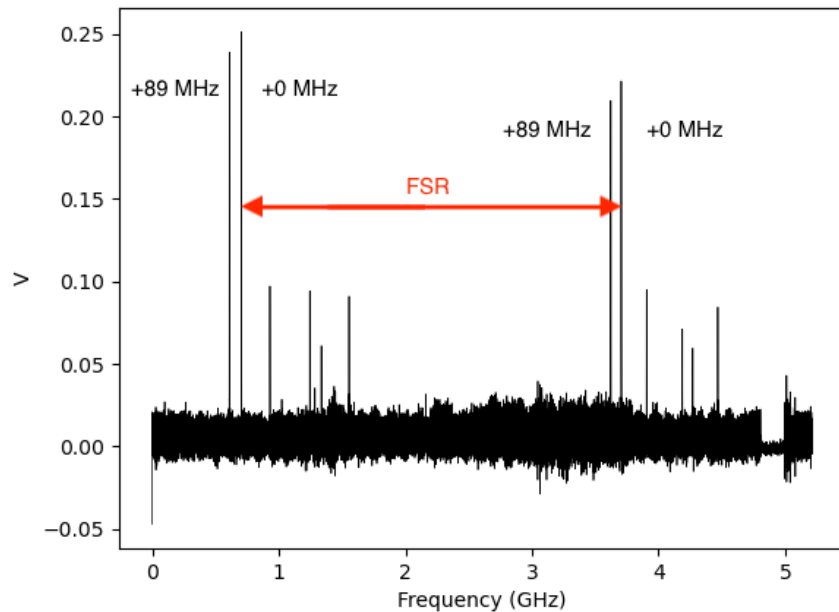

FIGURE 4.2: The photodiode at the end of the cavity outputs a signal with the following plot showing peaks from the AOM (+89 MHz) and the unmodulated (+0 MHz) beam. The cavity is scanned with a sawtooth signal and so the dip seen at $\sim$ 4.8 GHz corresponds to the end of the scan range. In this range two longitudinal modes are seen, indicated by the FSR. Alignment into the cavity was such that the most power was seen in these longitudinal modes with the transverse modes following from these two large peaks.

The first peak of amplitude ~ 0.23 V corresponds to the modulated beam from the AOM with the second peak of amplitude ~ 0.25 V to the unmodulated beam. The data from the photodiode in the cavity was sent to a picoscope. This has a readout rate which the x axis of the plot in Figure 4.3 shows as sample number. Identifying the FSR allowed for a frequency scale to be implemented. The length of the cavity L was 50 mm and so the FSR was 3 GHz as given by $c/2L$. The length of the cavity was scanned 100 times with a plot of all scans seen in Figure 4.4. A zoom in on one of the peaks shows the deviation in the central position of the peak. For each of the four peaks labelled in Figure 4.2, the average in sample number was taken such that the separation between the modulated and unmodulated beams for both longitudinal modes was averaged. The data is presented in Table 4.1.

TABLE 4.1: The average FSR in terms of sample number which corresponds to a frequency of 3 GHz. Average separation of modulated and unmodulated frequencies for the first pair of longitudinal modes (1, 2) and the second (3, 4).

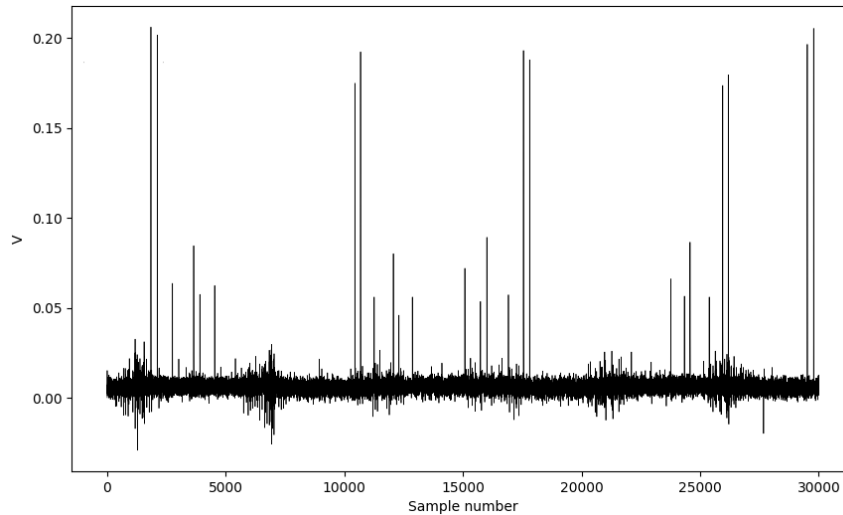|	Average FSR	Average shift (1, 2)	Average of shift (3, 4)
Sample number	17300 ± 100	600 ± 100	500 ± 100
Frequency (MHz)	3×10^3	95.2 ± 0.1	83.0 ± 0.1

FIGURE 4.3: A scan of the cavity with a triangular wavefunction shows that the two pairs of longitudinal modes are approximately symmetric around the centre of the plot.

Calculation of errors was done using the standard error of the mean given by $\sigma/\sqrt{N}$, where σ is the standard deviation of the sample numbers in a given peak and N the number of data points in the peak. When calculating a frequency shift, errors in the two peak positions were added in quadrature. The average FSR in terms of sample numbers is presented in Table 4.1 and corresponds to a shift of 3 GHz. The average separation of modulated and unmodulated frequencies for the first pair of longitudinal modes (1, 2) and the second (3, 4) were calculated. When converted to a frequency shift, values of (95.2 $\pm$ 0.1) MHz and (83.0 $\pm$ 0.1) MHz were obtained, which when averaged gave a shift of (89.1 $\pm$ 0.2) MHz.
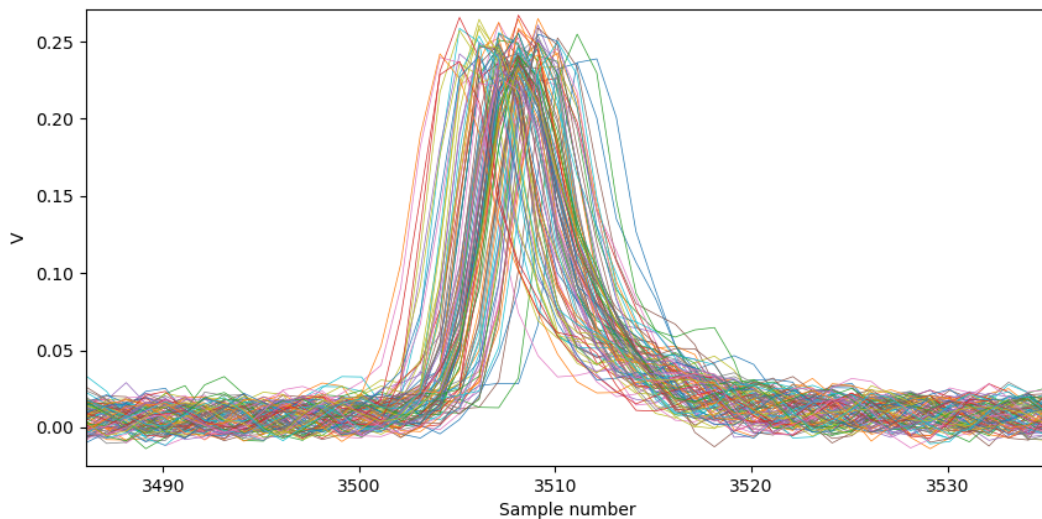

FIGURE 4.4: A zoom in on the first longitudinal mode of the modulated frequency with 100 scans plotted. The central position of the peak varies around the sample number 3510. Averaging over these peaks gave a mean sample number of 3507 $\pm$ 0.1.

4.3 Discussion

Reducing the transverse velocity of the molecular beam in a short duration of time, requires a high scattering rate of photons per molecule. A combination of perfectly tuned laser frequencies and a high laser power can be used to achieve this [24]. Therefore, the diffraction efficiency of the AOM should be maximised such that this high power can be realised. A maximum diffraction efficiency of 45% was obtained for the power directed to the + 89 MHz first order. For current fluorescence detection, a laser with a power in the range of 10 to 100 µW at the setup is required, any more than this results in power broadening. Taking this into consideration, a maximum diffraction efficiency of 45% is sufficient to achieve the power required. Alignment into the AOM can be adjusted to improve the efficiency if needed, however increasing the power of the laser can similarly optimise the power in the first order. To avoid damaging the crystal, the intensity of the laser should not exceed the maximum optical power density of 250 W/mm^2 permitted for the AOM.

A scan using a sawtooth wavefunction and then a triangular wavefunction showed two longitudinal modes per scan as seen in Figures 4.2 and 4.3 respectively. The results of the cavity scan presented in Table 4.1, show that the shift in frequency between both modulated and unmodulated frequencies is not equal for the two longitudinal modes. Furthermore, both shifts of (95.2 ± 0.1) MHz and (83.0 ± 0.1) MHz are within the order of ± 10 MHz from the value of 89 MHz. The linewidth of the laser used is 1 MHz and so drift from the laser does not account for this. Similarly, the drift due to the signal generator[3] is small and so error must arise from the scanning of the cavity. The non-linearity in the scanning of the cavity by the piezo means that applying a linear scale obtained from the FSR value is what results in both of these shifts differing. To account for this, the scan of the cavity could be extended such that the acceleration and deceleration of the piezo at the start and end of a scan can be analysed and compared with data taken towards the middle of this scan range.

Addressing a second hyperfine level in the ground state of BaF presents a move towards optical cycling and eventually Doppler cooling of BaF. The cooling of a beam of BaF in one-dimension has been shown by Y. Zhang et al [42]. The conclusion from this research found that cooling is still limited by the scattering rate of molecules before decaying to dark states. Therefore, they propose to close the $\nu = 2$ vibrational state as well as leaks to the intermediate $A'^2\Delta$ excited state. For this experiment, leakage to the dark m_F states formed in the $F = 2$ ground hyperfine level should be addressed. This can be done by destabilisation of the dark states using a small magnetic field or by switching quickly between linearly and circularly polarised light. Addressing these leaks would mean that BaF can be laser cooled efficiently such that the cold and parallel beam of molecules produced, is suitable for the eEDM measurement of the NL-eEDM group.

For future work, the remaining two ground hyperfine levels of BaF are left to be coupled to the $A^2\Pi_{1/2}$ ($\nu = 0, N = 0, J = 1/2$) excited state. This can be implemented with AOMs used to target the different frequency shifts required for excitation as shown in Figure 2.9. Targeting the $\nu = 1$ and $\nu = 2$ vibrational levels of the ground state with repump lasers such that vibrational decay is also addressed, further improves the total number of scatterings that can be achieved before a molecule enters a dark state. Recent research has resolved the splitting of the $F = 0$ and $F = 1$ hyperfine levels of the $A^2\Pi_{1/2}$ excited state as 18 MHz [43]. Such a relatively large splitting means that excitations to both hyperfine levels should be taken into consideration, as well as which transitions to each hyperfine level are strongest.

---

[3]DSG800 SERIES: RF SIGNAL GENERATOR

4.4 Conclusion

The objective of the work presented was to target a second hyperfine level of the $X^2\Sigma^+$ ($\nu = 0, N = 1$) ground state in BaF as shown in Figure 2.9. An optical setup with an AOM was used to shift to the frequency required for targeting the $F = 0$ hyperfine level of the ground state. Careful alignment involved adjusting the angle and height of the laser beam into the AOM as well as ensuring the beam waist was centered at the crystal. The frequency shifted first order beam could then be selected and combined with a second frequency which targets the $F = 1$ hyperfine level. In order to confirm that a beam with a frequency shifted by + 89 MHz had been coupled into the final laser beam, an optical cavity was used. By analysing the modal frequencies produced in the cavity, the FSR could be identified and a value assigned to the shift seen between consecutive modulated and unmodulated modes. Upon averaging repeated scans of the cavity it was found that a frequency shift of (89.1 ± 0.2) MHz was contained in the beam. These two frequency components be can used to target the $F = 0$ and $F = 1$ hyperfine levels of the ground state to improve the detection signal from LIF and present a move towards the laser cooling of BaF.

Acknowledgements

I would like to thank Steven and the eEDM group for giving me the opportunity to work on such an exciting project. It was the highlight of my bachelor study with all of the insight I gained into optics and how to conduct scientific research. I know that I would not have enjoyed my time as much without the friendliness of both the slow beam and nanospheres group. Thank you to Joost and Anno for supporting me throughout the project and making a safe space for questions! I will miss the sense of humour that you both bring to the lab. I would also like to thank Bastiaan and Vito for making our time in the fish bowl so enjoyable.

Bibliography

[1] R. Mann. *An Introduction to Particle Physics and the Standard Model*. 1st ed. CRC Press, 2009, pp. 18–20.

[2] S. Abachi et al. "Observation of the Top Quark". In: *Physical Review Letters* 74.14 (1995), pp. 2632–2637. DOI: 10.1103/physrevlett.74.2632.

[3] J. Gribbin and M. Gribbin. *Q is for Quantum*. Touchstone, 2000, pp. 155–156.

[4] R. Mann. *An Introduction to Particle Physics and the Standard Model*. 1st ed. CRC Press, 2009, pp. 483–484.

[5] A. Dobado et al. "Gravity and the Standard Model". In: *Effective Lagrangians for the Standard Model* (1997), pp. 229–257. DOI: 10.1007/978-3-642-59191-4_1.

[6] H. R. Quinn. "The Asymmetry Between Matter and Antimatter". In: *Physics Today* 56.2 (2003), pp. 30–35. DOI: 10.1063/1.1564346.

[7] W. Cottingham and D. Greenwood. *An Introduction to the Standard Model of Particle Physics*. 2nd ed. Cambridge University Press, 2007.

[8] M. Pospelov and A. Ritz. "Electric dipole moments as probes of new physics". In: *Annals of Physics* 318.1 (2005), pp. 119–169. DOI: 10.1016/j.aop.2005.04.002.

[9] M. Kobayashi and T. Maskawa. "CP Violation in the Renormalizable Theory of Weak Interaction". In: *Progress of Theoretical Physics* 2 (), pp. 652–657. DOI: 10.1143/ptp.49.652.

[10] K. P. Jungmann. "Experimental tests of fundamental symmetries". In: *Hyperfine Interactions* 228.1-3 (2014), pp. 21–29. DOI: 10.1007/s10751-014-1037-4.

[11] W. N. Cottingham and D. A. Greenwood. *An introduction to the standard model of particle physics*. 2nd ed. Cambridge University Press, 2007.

[12] The NL eEDM collaboration. "Measuring the electric dipole moment of the electron in BaF". In: *The European Physical Journal* 562.72.11 (2018), pp. 355–360. DOI: 10.1140/epjd/e2018-90192-9.

[13] N. Fortson, P. Sandars, and S. Barr. "The Search for a Permanent Electric Dipole Moment". In: *Physics Today* 56.6 (2003), pp. 33–39. DOI: 10.1063/1.1595052.

[14] P. Aggarwal. "Production, deceleration and trapping of SrF molecules". English. PhD thesis. University of Groningen, 2021, pp. 6–7. DOI: 10.33612/diss.177484581.

[15] J. J. Hudson et al. "Improved measurement of the shape of the electron". In: *Nature* 473.7348 (2011), pp. 493–496. DOI: 10.1038/nature10104.

[16] ACME Collaboration. "Improved limit on the electric dipole moment of the electron". In: *Nature* 562.7727 (2018), pp. 355–360. DOI: 10.1038/s41586-018-0599-8.

[17] P. Haase et al. "Systematic study and uncertainty evaluation of P, T-odd molecular enhancement factors in BaF". In: *The Journal of Chemical Physics* 155.3 (2021), p. 034309. DOI: 10.1063/5.0047344.

[18] P. G. H. Sandars. "Measurability of the Proton Electric Dipole Moment". In: *Physical Review Letters* 19.24 (1967), pp. 1396–1398. DOI: 10.1103/physrevlett.19.1396.

[19] L. I. Schiff. "Measurability of Nuclear Electric Dipole Moments". In: *Physical Review* 132.5 (1963), pp. 2194–2200. DOI: 10.1103/physrev.132.2194.

[20]   J. van Hofslot. "Increasing the intensity of a slow molecular beam using an electrostatic hexapole". English. University of Groningen, 2021. URL: `https://fse.studenttheses.ub.rug.nl/26158/`.

[21]   A. Zapara. "Dynamics of molecular beams in a traveling-wave Stark decelerator". English. PhD thesis. University of Groningen, 2019. ISBN: 978-94-034-1647-2.

[22]   N. J. Fitch and M. R. Tarbutt. "From Hot Beams to Trapped Ultracold Molecules: Motivations, Methods and Future Directions". In: *Molecular Beams in Physics and Chemistry*. Springer, 2021, pp. 491–516.

[23]   N.J. Fitch and M.R. Tarbutt. "Laser-cooled molecules". In: *Advances In Atomic, Molecular, and Optical Physics* (2021), pp. 157–262. DOI: `10.1016/bs.aamop.2021.04.003`.

[24]   M. R. Tarbutt. "Laser cooling of molecules". In: *Contemporary Physics* 59.4 (2018), pp. 356–376. DOI: `10.1080/00107514.2018.1576338`.

[25]   P. Aggarwal et al. "Lifetime measurements of the $A^2\Pi^{1/2}$ and $A^2\Pi^{3/2}$ states in BaF". In: *Physical Review A* 5 (). DOI: `10.1103/physreva.100.052503`.

[26]   J. Almond. "Laser cooling of YbF molecules for an improved measurement of the electron electric dipole moment". English. PhD thesis. Imperial College London, 2017. DOI: `https://doi.org/10.25560/47910`.

[27]   S. Kang et al. "The suitability of barium monofluoride for laser cooling from *ab initio* study". In: *Molecular Physics* 114.6 (2015), pp. 810–818. DOI: `10.1080/00268976.2015.1121294`.

[28]   E. Berg et al. "Lifetime measurements of excited molecular states using a Ti:sapphire laser". In: *Molecular Physics* 79.4 (1993), pp. 721–725. DOI: `10.1080/00268979300101571`.

[29]   P. Aggarwal. "Production, deceleration and trapping of SrF molecules". English. PhD thesis. University of Groningen, 2021, p. 32. DOI: `10.33612/diss.177484581`.

[30]   R. Paschotta. *Acousto-optic Modulators*. June 2022. URL: `https://www.rp-photonics.com/acousto_optic_modulators.html`.

[31]   A. Goutzoulis, D. Pape, and S. Kulakov. *Design and Fabrication of Acousto-Optic Devices (Optical Science and Engineering)*. 1st ed. New York, NY: CRC Press, 1994, pp. 4–6.

[32]   amsTechnologies. *AOMO 3080-122 AO Modulator GH*. URL: `http://www.amstechnologies-webshop.com/media/pdf/db/9d/4a/AOMO-3080-122-AO-Modulator-G-H-Datasheet.pdf`.

[33]   M. Mazurenka et al. "4 Cavity ring-down and cavity enhanced spectroscopy using diode lasers". In: *Annual Reports Section "C" (Physical Chemistry)* 101 (2005), p. 100. DOI: `10.1039/b408909j`.

[34]   H. Rongqing and M. O'Sullivan. "Fiber Optic Measurement Techniques". In: 1st ed. Academic Press, 2008, pp. 14–16.

[35]   H. Lotsch. "A Scalar Resonator Theory for Optical Frequencies". In: *Optica Acta: International Journal of Optics* 12.2 (1965), pp. 113–136. DOI: `10.1080/713817935`.

[36]   R.A. Meyers. "Encyclopedia of Physical Science and Technology". In: 3rd ed. Amsterdam University Press, 2002, pp. 260–263.

[37]   M. Bitarafan and R. DeCorby. "On-Chip High-Finesse Fabry-Perot Microcavities for Optical Sensing and Quantum Information". In: *Sensors* 17.8 (2017), p. 1748. DOI: `10.3390/s17081748`.

[38]   K. Esajas. "Intense slow beams of heavy molecules to test fundamental symmetries". English. PhD thesis. University of Groningen, 2021. DOI: `10.33612/diss.170215126`.

[39]   R. Paschotta. *Resonator Modes*. Aug. 18, 2021. URL: `https://www.rp-photonics.com/resonator_modes.html`.

[40]   R. Paschotta. "Beam quality deterioration of lasers caused by intracavity beam distortions". In: *Optics Express* 14.13 (2006), p. 6069. DOI: `10.1364/oe.14.006069`.

[41]   ISOMET CORP. *Maximizing AO Diffraction efficiency*. URL: https://isomet.com/App-Manual_pdf/Maximizing%20DE.pdf.

[42]   Y. Zhang et al. "Doppler cooling of buffer-gas-cooled barium monofluoride molecules". In: *Physical Review A* 105.3 (2022). DOI: 10.1103/physreva.105.033307.

[43]   W. Bu et al. *Saturated absorption spectroscopy of buffer-gas-cooled Barium monofluoride molecules*. 2022. DOI: 10.48550/ARXIV.2202.02463. URL: https://arxiv.org/abs/2202.02463.